

1 **Abstract**

2 Salt marshes' resiliency depends on their effective capture and retention of mineral sediment
 3 from adjacent waters. We used simultaneous deployment of net-deposition tiles and oceanographic
 4 sensors to identify the timing and magnitude of sediment import/export to, and re-
 5 distribution within, a marsh in South San Francisco Bay. As the marsh had both an erod-
 6 ing bay-exposed scarp and dominant tidal creek, we investigated the mechanisms and mag-
 7 nitudes of sediment import from the marsh-bay versus the marsh-creek interface. The strong
 8 daily sea breezes of the summer season drove most of the waviness that eroded the marsh
 9 scarp and controlled suspended sediment concentrations; the winter season was calmer, punc-
 10 tuated by only a few storms. The large seasonal difference in suspended sediments influenced
 11 both flood and ebb sediment fluxes in the marsh and led to much higher rates of import in
 12 the summer. Both bay-side and creek-side processes were important to marsh import. Bay-
 13 side processes were more variable due to the bay-influenced environment, and creek-side con-
 14 tributions were overall larger, reflecting the large proportion of the marsh fed by creek wa-
 15 ter. Close to the bay, sediment was frequently eroded from the marsh edge and transported
 16 towards the marsh interior. While there was also some sediment redistribution over the creek
 17 transect, the creek banks were characterized by rapid sediment accumulation. The interior
 18 of the marsh was less dynamic than the boundaries and accreted sediment slowly. The marsh
 19 complex was net importing sediment in the summer and exporting in the winter from dif-
 20 ferent rates of vertical accretion and edge erosion; on an annual scale, the marsh was net im-
 21 porting.

22 **1 Introduction**

23 Salt marshes are valued for the ecosystem services they support, including coastal pro-
 24 tection, rapid carbon sequestration, critical bird and fish habitat, and chemical pollutant re-
 25 moval (Barbier et al., 2011). A marshland's effectiveness in these capacities depends on its
 26 landform extent, shape, and function, in addition to exchange between the marshland and
 27 systems around it. Suspended sediments from adjacent waters are introduced to coastal salt
 28 marshes (often via tidal inundations); the sediment fluxes across the marsh control sediment
 29 retention and geomorphic change. When vegetated marshlands have sufficient sediment sup-
 30 ply and appropriate hydrodynamic conditions for deposition, they accumulate sediment as
 31 it settles during periods of slow flow. Tidal creeks are known to carry suspended material,
 32 but growing literature has questioned the primacy of creeks as the main conduit for sediment

33 (Coleman et al., 2020) or highlighted the role of flows directly over the marsh-bay bound-
 34 ary (Lacy et al., 2020).

35 Marsh-bay interfaces are subject to some dynamics not present at more protected marsh-
 36 channel interfaces. Erosion of the marsh-bay boundary by wave action has been identified
 37 as a source of sediment and, following resuspension by waves or tides, associated with de-
 38 position on the marsh-top platform (Nowacki & Ganju, 2020; Hopkinson et al., 2018; Mar-
 39 iotti & Carr, 2014). The majority of this deposition typically occurs close to the marsh bound-
 40 ary, but shifted up to tens of meters inland due to wave activity at the marsh edge (Duvall
 41 et al., 2019; Elsey-Quirk et al., 2019; Lacy et al., 2020). Distance to tidal creek is also ma-
 42 jor control on marsh-top sediment deposition rates (Moskalski & Sommerfield, 2012; Reed,
 43 1988), but without the wave-affected region. The stability of tidal channel morphology has
 44 been associated with sediment remaining local between bank failure events (Gabet, 1998),
 45 but wave-exposed marsh edges are generally not morphologically stable (Kirwan & Murray,
 46 2008). Because the pathways for suspended sediment to reach the marsh-bay edge are open
 47 to the complexities of the wave-influenced bay or estuarine system (Lacy et al., 2018), the
 48 relative importance, mechanisms, and net effects of bay-edge sediment pathways merit deeper
 49 study (Smith et al., 2021).

50 The need to improve predictability of marsh erosion and deposition on short timescales
 51 grows in response to rapid climate change and land use change, and to an increasing num-
 52 ber habitat restoration projects in these valuable ecosystems. However, the slow and accu-
 53 mulative dynamics of sedimentation are often difficult to rectify with the more rapid hydro-
 54 dynamics. Effective marsh restoration and management plans are addled by both sediment
 55 resources (Ganju, 2019; Liu et al., 2021), which are increasingly low (Larsen & Milligan, 2023),
 56 and the limited utility of decadal-scale trends (Smith et al., 2021). Well-established concep-
 57 tual models of short-term marsh sediment deposition dynamics (Lacy et al., 2020) and link-
 58 age between short-term dynamics and sedimentation needs for resiliency to sea level rise are
 59 generally missing (Schile et al., 2014; Stralberg et al., 2011).

60 In this paper, we examine sediment import, deposition, and redistribution patterns on
 61 tidal, spring-neap, and seasonal timescales in a Mediterranean-climate salt marsh undergo-
 62 ing rapid wave-driven lateral retreat. We compare the relative contributions of import from
 63 the bay-edge and creek-edge to total marsh-top sedimentation. Using a combination of net
 64 deposition tile observations and timeseries data from marsh-top sensors, we compare sed-

iment deposition patterns between the marsh boundary (both bay and creek) and marsh interior. These two regimes highlight the impact of distance from the “sediment-contributing edge” to deposition patterns. We explore sediment transport dynamics in these regimes using the shorter-timescale sensor data. Using other published data at the site—marsh-edge retreat rates and sediment fluxes through the tidal creeks—we calculate a coarse sediment budget of fluxes through marsh system.

71 2 Study Site

72 Our study site was Whale's Tail Marsh South (WTMS), a small (0.51 km^2) high marsh
 73 along the eastern shoreline of South San Francisco Bay (SSFB, Fig. 1.A). The marsh is bound
 74 by levees to its north, east, and southeast, and open to SSFB to its west and south (Fig. 1.B).
 75 On the marsh' eastern side, the levee was breached to allow a 15 m-wide tidal creek to flow
 76 into a smaller (0.19 km^2) marsh region, dubbed the Cargill Pond. Cargill pond is also con-
 77 nected to WTMS by a second opening (3.5 m-wide and shallower) near the north end of the
 78 boundary between the two marshes. Together, we refer to this two-marsh system and its tidal
 79 creeks as the “marsh complex”. WTMS is fed by waters directly from SSFB as well as from
 80 the primary tidal creek from the marsh' southeastern corner, which feeds smaller creeks. The
 81 complex is disconnected from any freshwater flows from upland.

82 The marsh-top platforms were largely covered in a dense vegetated mat of *Salicornia*
 83 *pacifica* (“pickleweed”), with occasional *Grindelia stricta* var. *angustifolia* (“marsh gum plant”)
 84 and some other species along higher channel margins. On July 28th 2021 and January 25th
 85 2022, we performed vegetation surveys along our study transects: pickleweed ranged from
 86 3 to 18 cm tall with averages of 11 and 9 cm in the summer and winter, respectively. The
 87 marsh-top platform was effectively unvegetated within 1-2 m of the bay-edge and cover in-
 88 creased to 90-100% at stations more than 6 m inland of water edges. Further details are in-
 89 cluded in Thorne and Bristow (2023).

90 Five digital surface models (DSMs) of the study region were collected across a study
 91 year from May 2021-May 2022 and published in Logan et al. (2023), allowing us to quan-
 92 tify the site geomorphology. The approximately 1.1 km-long open-water western edge of WTMS
 93 is characterized by a steep escarpment or “scarp,” typically about 1-1.5 m tall, separating
 94 unvegetated tidal mudflats from the vegetated marsh-top surface (Fig. 1.D). The marsh-top
 95 platform is typically between 2.0 and 2.3 m in elevation, with two remnant levees which are

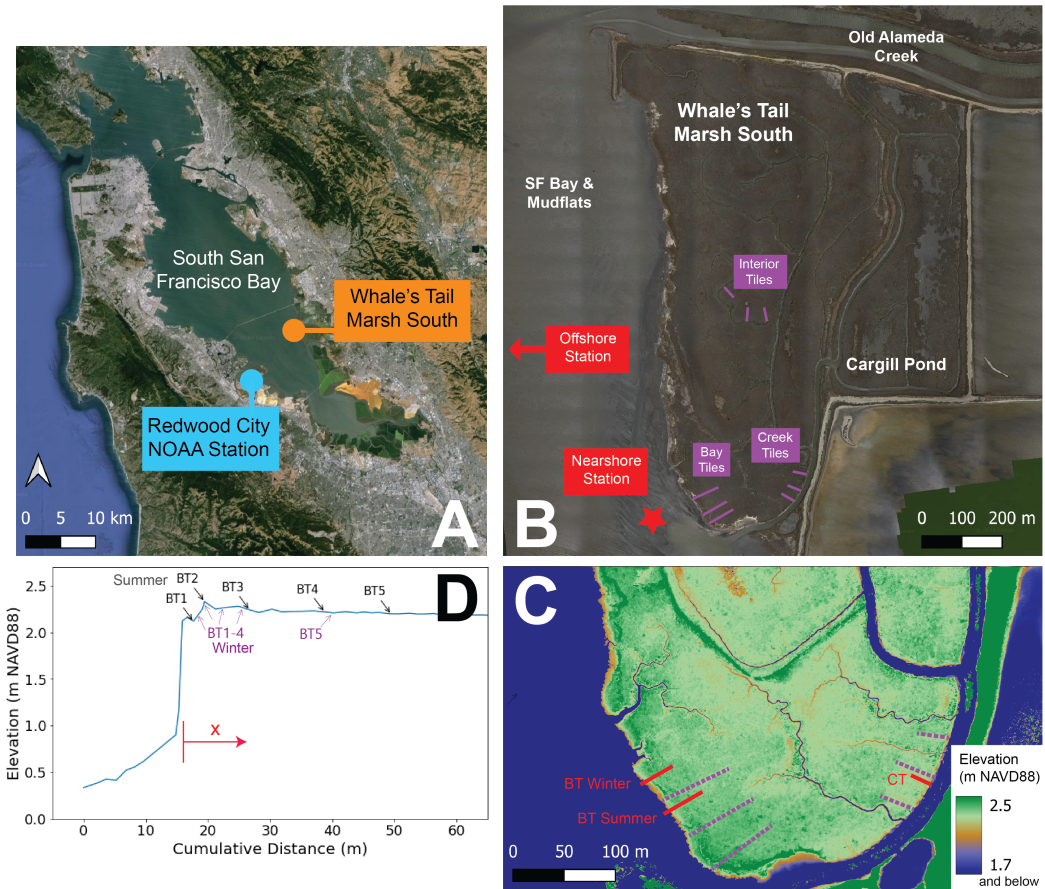


Figure 1. (A) Locations of the marsh complex (orange) and nearby tide gauge (light blue) within South San Francisco Bay. (B) Aerial orthomosaic image of the marsh complex in May 2021, with bay waters to the west. Purple lines indicate transects of net deposition tiles; red items indicate sensor locations. (C) Topographic map from a digital surface model of the southern end of Whale's Tail Marsh from the same date as the previous panel. Dotted purple lines indicate where the tile transects are, and red solid lines indicate the locations of marsh-top sensor transects. BT = Bay Transect; CT = Creek Transect. The creek transect did not change locations between seasons. (D) A representative cross-sectional profile going from adjacent mudflats on to the marsh-top platform, with distances of BT sensor locations displayed.

closer to 2.3-2.5 m (NAVD88, Fig. 1.C). The naturally high-elevation portions of the marsh are in subtle natural levee forms along the bay boundary. The naturally low-elevation portions of the marsh are typically at the heads of the tidal creek fingers. The surface models represent the top of the vegetation canopy rather than bare earth. From RTK GNSS data collected by walking the marsh platform in southern WTMS on December 1st 2021, we found an average 0.22 m offset between the DSM surface and marsh ground surface, consistent with vegetation offsets found across San Francisco Bay by Buffington et al. (2016). Thus this suggests the bare-earth marsh-top platform is at around 2.2 m (NAVD88). Offshore of the marsh region, below the scarp, is more than a kilometer of intertidal mudflats, generally below 0.4 m (NAVD88).

The tides in San Francisco Bay are mixed semidiurnal. As measured at the NOAA Redwood City station on the western side of SSFB (Fig. 1.A), mean higher-high water is at 2.14 m and mean lower-low water at -0.36 m (NAVD88) although our study suggested regular slightly higher total water elevations at WTMS. Thus, the marsh-top platform only gets inundated during tides at the upper end of the tidal range, and occasionally not at all during neap periods in the tidal cycle. Given that WTMS is enclosed within SSFB, it is protected from open-ocean waves; we assume all waves at the site have been generated by local winds. During the spring and summer months, there is regularly a daily sea breeze from the WNW up to around 6 m/s which begins in late morning or early afternoon and abates in the late afternoon or early evening (Conomos et al., 1985). There are occasional winter storms in SSFB; those in our study period came from the S-SW with winds of 5-10 m/s. The winter storms are known to incur regional pulses of suspended sediment (Barnard et al., 2013).

3 Methods

3.1 Net Deposition Tiles

Sediment deposition traps, deployed as triplicate 10 × 10 cm tiles staked into the marsh surface with circular borosilicate (or, where very wave-exposed, rubber) filter pads attached by crosshatched rubber bands, were installed at seven (six) distances from bay (creek) edges in both seasons near the instrumented transects. A third transect of six tiles at an interior creek—in the center of Fig. 1.B—was also deployed in both seasons. The bay-edge transects were 72 meters long, and the creek-side transects were 30 meters long. Tiles were collected and replaced four times, every two weeks (roughly two spring/neap cycles) during each sen-

127 sor deployment; further tile deployment details are available in Thorne and Bristow (2023).
 128 We assumed that all deposition observed on the tiles was allochthonous sediment introduced
 129 by tidal inundation. These samples were measured for mass accumulation and % carbon.

130 To quantify total deposition rates over the entire marsh, we fit tile deposition rates on
 131 to curves, $D(x)$, as functions of distance from body of water x (bay, primary creek, or in-
 132 terior creek). Given spring and neap periods, two seasons, and three regions, there were a
 133 total of 12 $D(x)$ equations. When no net deposition was found at the two stations closest
 134 to the bay-side edge—which we interpreted as an erosional region—we did not include the
 135 tiles in curve-fitting and x values were shifted inland. For the two creek tile transects (pri-
 136 mary creek & interior), we fit $D(x) = ae^{-bx} + c$ functional forms; at the bay, we fit a $D(x) =$
 137 $axe^{-bx} + c$. To attribute sediment deposited in a given location to a source of water, we
 138 drew the bay edge and the channel boundaries which remained wet during low tides from our
 139 aerial imagery. The marsh-top surface was then divided into sections associated with the most
 140 proximal water edge, and deposition rates were calculated for each square meter based on
 141 the distance to that edge using the appropriate functional form for each section. More de-
 142 tails about this sectioning is available in A1. We calculated deposition rates across the en-
 143 tire marsh (for the sediment budget, Sec 5.1) using the average of spring and neap $D(x)$ -
 144 derived values.

145 3.2 Sediment Characterization

146 We collected short push-cores of bed sediments (usually a few centimeters deep) from
 147 the shallows of SSFB near the marsh in each study season, proximal to sensor locations. Each
 148 push-core was taken with a 37 mm diameter corer and sectioned into 0.5 cm sections down
 149 to 1 cm, then 1 cm sections below. Each sample was analyzed for grain size distribution, bulk
 150 density, total inorganic carbon, and total organic carbon, with more process details included
 151 in Ferreira, McGill, et al. (2023). We used only the top-most section near our sensor loca-
 152 tions as representative of labile sediment for this study.

153 We also collected shallow cores on the marsh-top at each sediment tile location. These
 154 samples were sectioned at 0.5, 2, 4, and 6 cm depths and analyzed for bulk density and loss-
 155 on-ignition (transformed to total organic carbon), with process details in Thorne and Bris-
 156 tow (2023). We discuss only the top 0.5 cm sections of these as well. A 70 cm core was taken

157 horizontally from the mudflats into the marsh boundary in the center of the scarp, to char-
 158 acterize the sediment eroding from the marsh scarp.

159 On July 28th 2021, we took sediment deposited on the 6 and 24 m (0.5 and 24 m) tiles
 160 on the bay-side transect (creek-side) for grain size distribution analysis. These were the same
 161 tiles as from Sec. 3.1 but we collected the sediment *not* on the pads—sediment not used to
 162 quantify deposition rates.

163 3.3 Sensor Deployment & Data Processing

164 We deployed instruments in the mudflats fronting the marsh, with one offshore sub-
 165 tidal “mudflat” station and one intertidal “nearshore” station, about 2.3 km and 110 m from
 166 the marsh shoreline, respectively, to capture in-bay forcing conditions to the marsh (Fig. 1.B).
 167 On the marsh top, we deployed transects of co-located turbidity and pressure sensors going
 168 from the marsh edge into the interior staggered with the sediment tiles (red lines in Fig. 1.C)
 169 at the bay-edge and creek-edge. The bay-edge transect had five stations (BT1-5) and the
 170 creek-edge transect had four (CT1-4). This deployment strategy was performed twice, a 7
 171 June - 11 August 2021 summer deployment and a 23 November 2021 - 31 January 2022 a
 172 winter deployment. In this paper we only discuss burst-mean data, although higher-frequency
 173 data are available in Ferreira, Lacy, et al. (2023). Station names and data types collected
 174 at each are clarified in Table 1. The transect along the primary creek of WTMS was 12.2
 175 m long in both seasons. The bay-edge transect was 34 m long in the summer, but in the win-
 176 ter it was shifted approximately a meter inland for more wave protection, shortened to 24
 177 m, and moved northward slightly (see Fig. 1.C). Real-time kinetic GNSS surveys were used
 178 to measure the location and elevations of instruments on installation. Because the sensors
 179 were a few centimeters (2-11 cm) off of the ground surface to function properly and varied
 180 in absolute elevation, extremely shallow marsh inundations were not captured, and some sen-
 181 sors registered different inundation durations than others. BT2 (BT3) in the summer (win-
 182 ter) were at slightly higher elevations than their peers due to a subtle bay-edge levee fea-
 183 ture (visible in 1.D). Nearshore and mudflat sensors were 25 cm above bed.

184 Pressure values collected by the sensors were adjusted for local atmospheric pressure
 185 before conversion to water depths and water surface elevations. Wave properties were cal-
 186 culated following methods in Wiberg and Sherwood (2008). Further detail on the sensor de-

Station Name(s)	Location	Metrics Collected	Sampling Regime	Elevation (m NAVD88)
BT1, BT2, BT3, BT4, BT5	Linear array on marsh-top at bay-edge	Pressure, Turbidity, Spectral Wave Properties	1024 samples, 6 Hz, every 5 min. / 2.05 2.15, 2.27, 2.26, 2.24 winter	2.12, 2.33, 2.24, 2.22, 2.20 summer / 2.05 2.15, 2.27, 2.26, 2.24 winter
CT1, CT2, CT3, CT4	Linear array on marsh-top orthogonal to primary creek	Pressure, Turbidity	10 samples, 1 Hz, every 5 min. / 2.09, 2.10, 2.17, 2.18 winter	2.13, 2.18, 2.19, 2.19 summer / 2.09, 2.10, 2.17, 2.18 winter
“Nearshore” (MES)	110 m offshore of SW corner of WTMS	Pressure, Turbidity, Spectral Wave Properties	2080 samples, 8 Hz, every 15 min.	0.31 both seasons
“Mudflat” (BMV)	2.3 km west of central WTMS edge	Pressure, Turbidity, Spectral Wave Properties, Velocities	2080 samples, 8 Hz, every 15 min.	-1.03 summer, -0.81 winter

Table 1. Information about sensor deployments from both seasons. BT1-5 at the bay transect and CT1-4 at the primary creek transect were marsh-top stations and only inundated at higher high tides (≥ 2 m, NAVD88), whereas “MES,” the nearshore station, was intertidal (0.3 m, NAVD88), and “BMV” was just barely subtidal (-1 m NAVD88), with some very low-depth data removed.

187 placements and data produced is available in Ferreira, Lacy, et al. (2023); in Sec. A2 we ex-
 188 plain how we adjusted for temperature-based aberrations in pressure records.

189 All optical backscatter-based turbidity measurements were calibrated to suspended-sediment
 190 concentration (SSC) values via water samples. Water samples were pumped with the inlet
 191 co-located with the sensors, recording data, held over the side of a boat in the shallows near
 192 the marsh on days before and after deployment. The calibrations used between 19 and 29
 193 points from both summer and winter samples, because individual-season regressions were not
 194 significantly different and winter sampling periods were generally very low in SSC. The zero-
 195 intercept linear regressions had R^2 values between 0.73 and 0.99, and all from the marsh-
 196 top were >0.9 .

197 3.4 Marsh-top Inundation Periods & Fluxes

198 Intertidal marsh-top sensor timeseries data were decomposed into individual inunda-
 199 tion periods via an algorithm using both pressure and SSC timeseries at each station to iden-
 200 tify inundations. Details on this process are available in A2. Each inundation was split into
 201 “flood” and “ebb” periods by the time of deepest inundation and mean SSC values were found
 202 for each. (Tides are close to standing waves at the field site.) We assumed the water col-
 203 umn was well-mixed, thus the measured SSC values were representative of the entire column.
 204 Single-burst outliers of SSC at the beginning and ends of inundations were removed and at-
 205 tributed to glare or debris on the optical backscatter sensor during shallow water.

206 We used a “deposition potential” (DP) metric to represent the potential for a given
 207 inundation to deposit sediment, assuming that the sediment column does not clear and in-
 208 stead deposition is governed by sediment concentration and the available time for settling.
 209 Thus, $DP_i = \overline{SSC}_i * T_i$ where for inundation i , \overline{SSC}_i is the inundation-mean SSC, and
 210 T_i is the inundation duration. DP_i values over two-week periods were summed for compar-
 211 ison with observed tile-based deposition metrics, which were linearly interpolated to the sen-
 212 sor locations.

213 For each inundation at each marsh-top sensor, we calculated suspended sediment flux
 214 (SSF) values. This assumed inland “import” during flood tides and offshore “export” dur-
 215 ing ebb tides. On each inundation, we calculated the volume of water that would flow past
 216 a given sensor using the area inland of a sensor attributable to the bay or creek and the max-
 217 imum depth reached during the given inundation. We then divided by the length of the in-

undated perimeter to obtain per-unit-width volume flux measurements. We multiplied these water volume flux measurements by the flood- or ebb-mean SSC to find $SSF_{n,i,s}$, where n is station number (example: BT1 is $n = 1$), i is inundation number, and stage s could be flood or ebb. For a given inundation, the net SSF was:

$$SSF_{n,i,\text{net}} = SSF_{n,i,\text{flood}} - SSF_{n,i,\text{ebb}} \quad (1)$$

We used the x-direction gradient in SSF values as a per-inundation indication of deposition or erosion following Lacy et al. (2020):

$$D_{n,i} = \frac{SSF_{n,i,\text{net}} - SSF_{n+1,i,\text{net}}}{\Delta x} \quad (2)$$

where Δx is the distance between adjacent stations. Thus positive $D_{n,i,s}$ is depositional between sensors, and negative is erosional.

Not all sensors were inundated in all periods of marsh inundation, thus there were inundations for which calculating $SSF_{n,i,\text{net}}$ and $D_{n,i}$ for all n was not possible. Additionally, the SSC record during the second set of summer spring tides at sensor BT3 was compromised due to debris which got stuck around the sensor head; these data were removed from analysis. Partial-transect data are still presented, with $D_{n,i}$ calculated between non-adjacent sensors in an analogous way (example: gradient between BT3 and BT5, when BT4 data were not available).

3.5 Mass Fluxes from Outside Sources

We relied on previous studies to quantify two elements of the sediment flux budget: the wave-driven erosion of the marsh at the bay-edge, and the flux through the primary channel into the Cargill Pond.

For lateral erosion rates, we calculated volumetric retreat rates as performed in WinklerPrins et al. (2024) but using a hand-drawn region tightly cropped to the marsh-edge, so as to exclude the mudflat and marsh-top surface. Within this area, we took the difference of elevations from digital surface models to find volumetric differences over summer and winter seasons, as well as over a year May 2021-May 2022. As these regions were effectively unveg-

242 etated, we expected little bias due to vegetation. To convert volumes to masses, we used a
 243 representative bulk density from the long core taken horizontally into the marsh scarp.

244 The rate of sediment import into the Cargill Pond region was calculated from suspended
 245 sediment flux measurements in the primary creek in summer and winter deployments across
 246 the main levee break (visible in Fig. 1.B near the words “Cargill Pond”), detailed in Nowacki
 247 et al. (2024).

248 4 Results

249 4.1 Tile-Based Deposition Rates

250 Deposition found on tiles generally decreased with distance from the nearest water source
 251 and reached small but nonzero values going inland, with some variation throughout the study
 252 periods (see Fig. 2). Spring-tide per-unit area deposition rates were highest at the creek-edge
 253 transect (up to nearly 300 g/m²/day), second-highest along the interior creek transect, and
 254 lowest at the bay-edge. Neap-tide period depositions had smaller differences between the sites.
 255 The two tiles closest to the bay-edge—within 2 meters—were often found with zero depo-
 256 sition, or with the sediment trap pad missing completely, strongly suggesting a net erosional
 257 environment; the peak deposition rates at the bay-edge transects were at the 6 m-inland tiles.
 258 At the two creek-edge transects, there were strong differences between higher near-shore de-
 259 position rates derived from spring tide periods versus lower deposition rates during neap tide
 260 periods. There was a strong seasonal difference, with very low—sometimes virtually zero—
 261 deposition measured in the winter (note the y-axis scale differences in summer versus win-
 262 ter in Fig. 2).

263 Applying the deposition model based on the $D(x)$ curves, we found the following whole-
 264 marsh sediment import rates in kg/day: +9425 / +2536 (spring/neap summer, average +6080)
 265 and +1696 / +346 (spring/neap winter, average +1022). These values are later separated
 266 into attribution from bay or creek (primary and interior) in Tbl. 2. If the summer/winter spring/neap
 267 total import rates were contributed equally over a year, WTMS would be importing an av-
 268 erage of +3500 kg/day in sediment annually. Approximately 54% of the WTMS marsh-top
 269 surface was attributed to the asymptotic tails in the $D(x)$ forms by this technique.

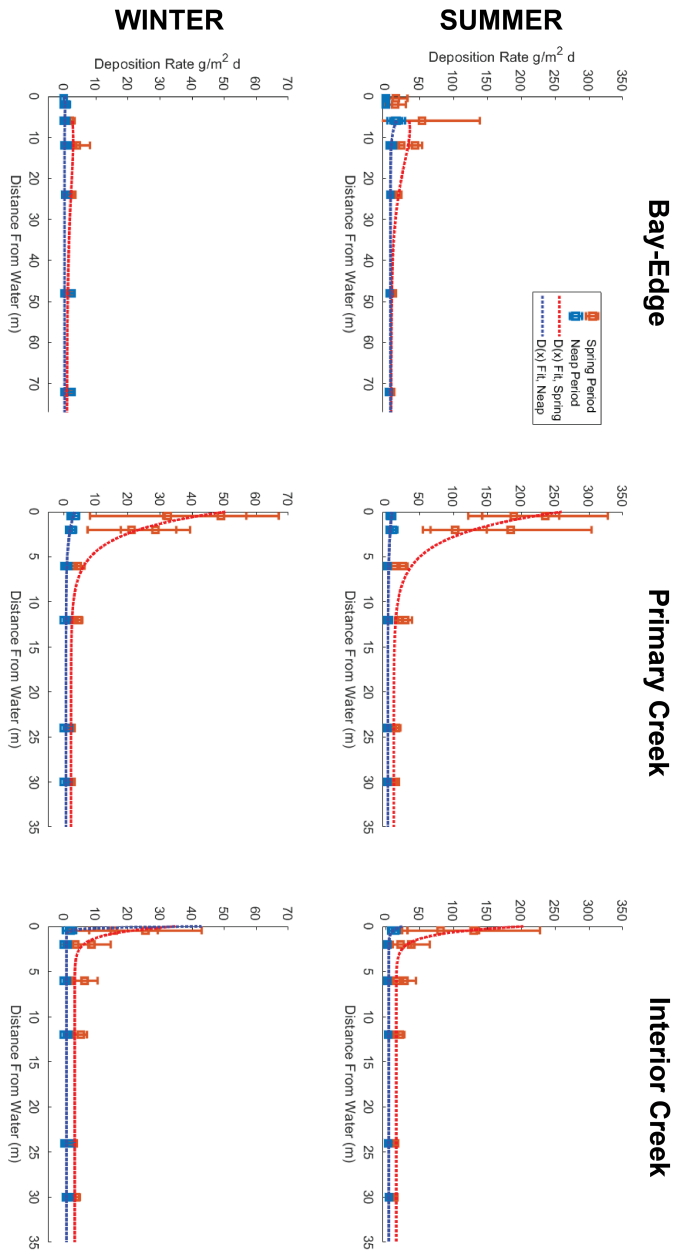


Figure 2. Mean deposition rates (with standard deviations from triplicates) found on net deposition tiles across all three sampling regions (bay-edge, primary creek, interior creek). Curves drawn to fit data, for use to extend the tile deposition observations across the entire marsh, are shown as dotted curves.

270 **4.2 Sediment Composition**

271 Sediment across the system was low in carbon. All samples from the mudflat and nearshore
 272 stations were <2% total carbon and <1% organic carbon. Samples from the marsh top had
 273 somewhat higher values, with 6-20% total carbon and average 11% organic carbon.

274 Sediment samples varied in size distributions across WTMS, although extremely few
 275 samples had anything coarser than coarse sand (1.68 mm median diameter) and none with
 276 anything finer than fine clay (0.00035 mm median diameter). The grain size distributions
 277 from samples at the mudflat station were 32-54% sand, 31-50% silt, and 10-21% clay. At
 278 the nearshore station, respective values were 67-93%, 4-22%, 3-11%, with slightly more sand
 279 fraction in the summer season.

280 Grain sizes from the marsh-top samples were very similar between 6 m from the bay-
 281 edge and 0.5 m from the creek edge. They matched and at 24 m from both edges as well.
 282 Closer to the edge, sand fractions were 17% and 12% at the bay and creek, respectively, 66%
 283 silt in both transects, and 17% and 23% clay, respectively. At the 24 m from edge tiles, sed-
 284 iment samples were both less than 1% sand, 66% and 61% silt from the bay and creek, then
 285 33% and 38% clay, respectively. Thus, sediments on the marsh-top platform were generally
 286 finer than those from the bay floor and shallows, particularly inland. The exceptions were
 287 two very sandy samples taken from the wave-influenced region immediately next to the bay
 288 (but not at tiles) in the summer: 90 and 99% sand, 6 and 0.5% silt, then 0.4 and 0.3% clay;
 289 a third sample was 22% sand, 45% silt, and 32% clay.

290 Bulk densities of the surface samples from the marsh top varied between 0.3 and 1.3
 291 g/cm³; their average was 0.71 g/cm³± 0.22 (standard deviation). The core from the marsh
 292 edge had an average bulk density of 0.60 g/cm³, with a smaller range, from 0.54 to 0.72 g/cm³.
 293 Samples from the nearshore and mudflat stations (and the two sandy marsh-top samples)
 294 had much higher bulk densities, between 1.1 and 1.8 g/cm³.

295 **4.3 Mudflat-Marsh Wave Characteristics**

296 As measured at the subtidal mudflat station, the summer season was characterized by
 297 waves generated locally by the daily sea breeze. These had short periods (<4 s) and typi-
 298 cally reached significant wave heights of 0.35-0.5 m in the late afternoon of every day. Out-
 299 side the sea breeze periods, wave heights were usually 0.2 m or less (Fig. 3).A). The win-

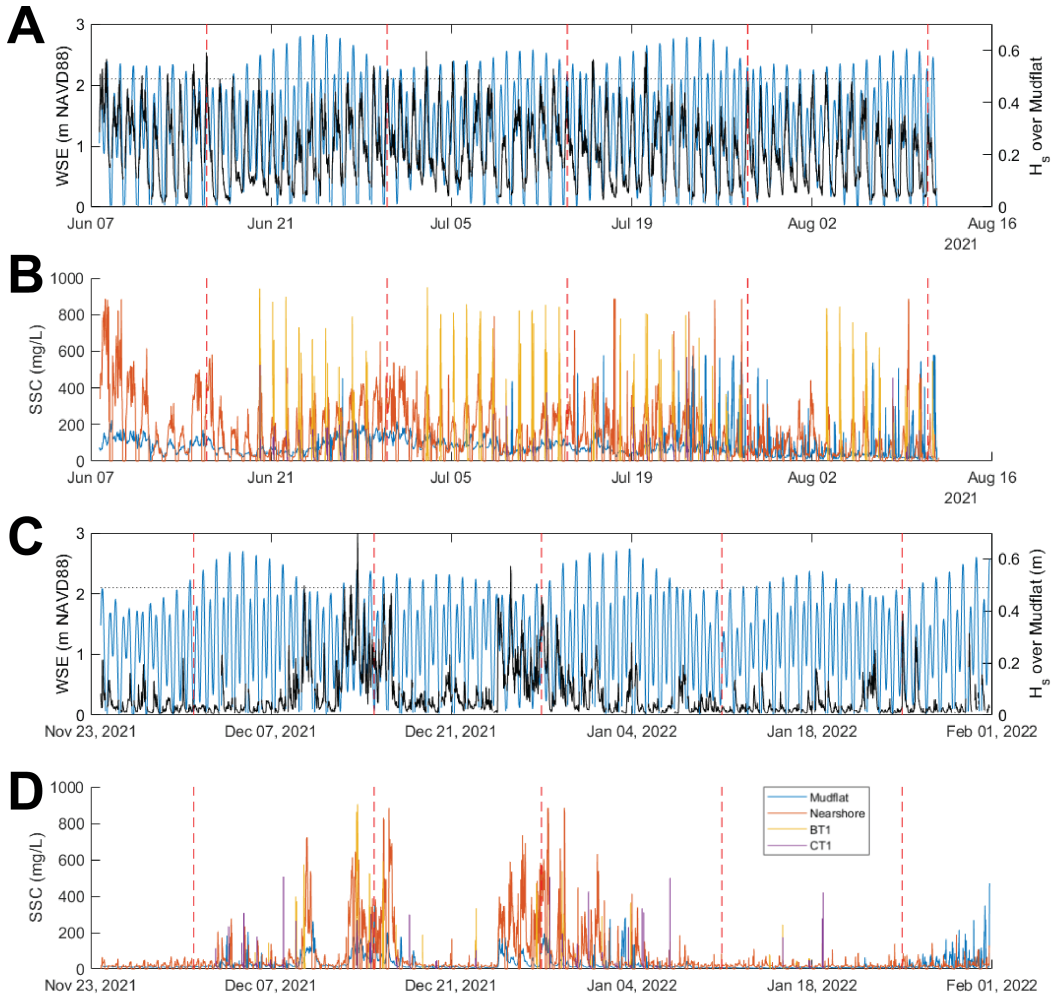


Figure 3. Timeseries of water depths and wave heights at the mudflat station are in panels A (summer) and C (winter); the approximate marsh-surface elevation is represented by a constant dotted line. SSC timeseries at the mudflat, nearshore, and first bay- or creek-edge marsh-top sensors (BT1 and CT1) are in panels B (summer) and D (winter). Red dashed vertical lines indicate times when deposition tiles were placed/replaced/removed.

300 ter season, typically had negligible wave heights (<0.1 m) but was punctuated by approx-
 301 imately five storms where significant wave heights exceeded 0.4 m; one storm had maximum
 302 significant wave height of 0.75 m (Fig. 3.C).

303 The marsh-top was only inundated at very high tides and sometimes not at all during
 304 neap tide periods. The lowest-elevation sensor on the bay transect, BT1, was inundated 40
 305 and 30 times in the summer and winter, respectively. The lowest-elevation sensors on the
 306 creek transect—CT1 in the summer, CT2 in the winter—were inundated 26 and 33 times,

307 respectively. Other sensors at slightly higher elevations were inundated less frequently, par-
 308 ticularly BT3-5. Hydroperiods were generally 2-3 hours, and creek-edge sensors typically reached
 309 peak water depths about a half hour after bay-edge sensors. H_s values over the marsh-top
 310 at the bay transect were small, nearly 0.2 m at maximum in the summer and winter seasons.
 311 Wave height decayed exponentially with distance into the marsh; during the waviest peri-
 312 ods, a $H = H_0 e^{-0.35x}$ form fit the data well, where H_0 was wave height at BT1. Assum-
 313 ing this form, waves decayed to 10% of their H_0 height within 7 m of the bay-edge. We did
 314 not measure wave metrics at the creek-side transect.

315 4.4 Suspended Sediment Dynamics

316 Suspended-sediment concentration (SSC) varied widely across tides and windy/wavy
 317 conditions, with strong seasonal differences. In the summer season, SSC at the mudflat sta-
 318 tion was often relatively constant between lower-high and higher-high water, sometimes
 319 with peaks during intermediate low water levels. SSC during lower-low water levels were less
 320 consistent and not always captured. In the winter season over the mudflats, SSC was over-
 321 all much lower, with elevated SSC data mostly driven by waviness. When captured by the
 322 sensors, lower-low water levels often correlated with peaks in SSC.

323 At the nearshore station in the summer, the SSC typically reached a high plateau dur-
 324 ing the lower-high tide and then a higher plateau during higher-high tides. The highest daily
 325 SSC typically occurred during higher-high tides (though was not always very pronounced),
 326 and these periods often occurred during afternoon sea breezes. In the winter season, SSC
 327 was also much lower than the summer except during wavy storm conditions (Fig. 3.C,D)—
 328 particularly when there was deeper water for wave development—and daily/tidal fluctuations
 329 in the sensor SSC records were muted. Occasionally there was a spike in SSC during higher-
 330 low water events. Many lower-low water events were not captured.

331 SSC magnitudes were almost always higher at the nearshore station than the offshore
 332 mudflat station in both seasons, but relationships between flood-average SSC at the nearshore
 333 sensor those of BT1 and CT1 were more nuanced. On a per-inundation basis, BT1 flood SSC
 334 responded variably to the nearshore SSC (Fig. 4, upper panel), although BT1 was typically
 335 more turbid than the nearshore sensor, with most points above the 1:1 line. The SSC at CT1,
 336 in contrast, was typically lower than that of the nearshore station (Fig. 4, lower panel), al-
 337beit with some agreement below 100 mg/L. These patterns were dominated by summer-season

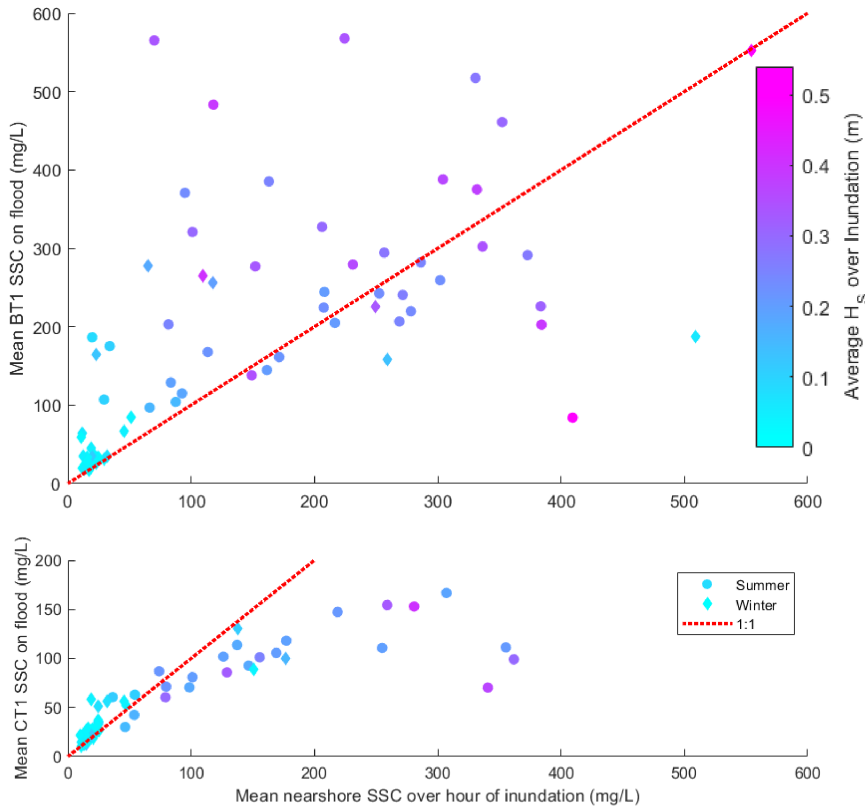


Figure 4. Mean flood-tide SSC values at BT1 (top panel) and CT1 (bottom panel) are plotted against the mean SSC at the nearshore station for the hour centered at the beginning of BT1/CT1's inundation. Each point represents one inundation, with summer inundations as circles and winter inundations as diamonds. Points are colored by the average H_s value at the mudflat station for the hour centered at the beginning of BT1's inundation.

inundations as SSC was very low during the majority of winter-season inundations. Both seasons had higher SSC at all sensors during wavier conditions (see symbol colors in Fig. 4). Linear regressions between nearshore SSC and the flood-mean SSC values at stations going further into the marsh—BT2-5, CT2-4—had less error than those of BT1/CT1, but lower slopes, all less than 1 (not shown).

SSC often increased from BT1 to BT2 and decreased from BT2 to BT3, before very gently decreasing further inland; SSC records of BT3-5 following very similar trajectories in time as evident in three example inundations in Fig. 5. SSC values across stations CT1-4 were typically very similar, with some spikes at CT2 or CT3. In both seasons and both transects, although more visible in summer due to higher sediment concentrations, SSC decreased dur-

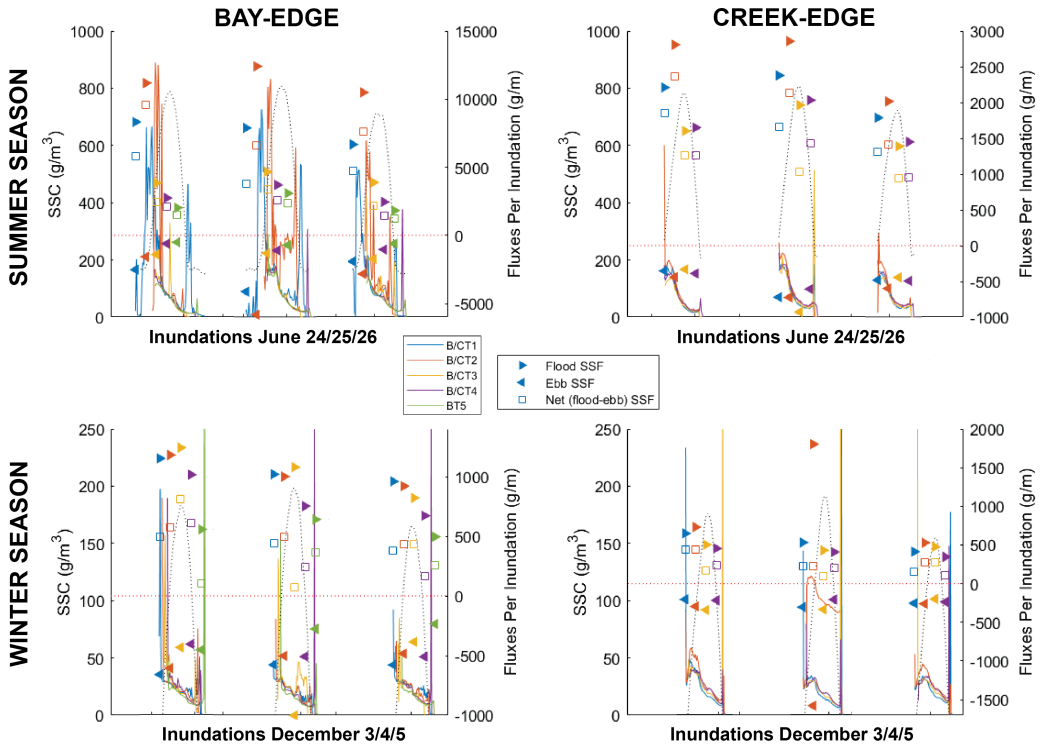


Figure 5. Snippets of timeseries from both seasons and transects. Triangle symbols represent per-inundation flood (right-pointing) vs ebb (left-pointing) SSF values, and empty square symbols represent the net SSF. Points are artificially staggered BT1-5/CT1-4 left-to-right for legibility; each cluster corresponds to a single inundation. These fluxes are contextualized by water surface elevation timeseries data from B/CT1 (black dotted lines, unscaled) and SSC timeseries at all sensors. Notice the common decrease in SSC signal over inundations and the relative differences across transects and seasons. Note y-axis scales of SSC and fluxes are not identical. Gaps in time between inundations have been removed for legibility.

348 ing each inundation, following a concave-up curve. Thus, flood-mean SSC was often a fac-
 349 tor of 1-3 higher than ebb-mean SSC, consistent with deposition in the marsh.

350 4.5 Marsh-Top Sediment Fluxes

351 Most sensor-based net flux (Eqn. 1) metrics for individual inundations were positive
 352 across all time and space: there was more suspended-sediment flux (SSF) on flood than ebb
 353 and thus net import into the marsh (Figs. 5, 6). Net flux values were typically much smaller
 354 than either flood or ebb SSF (Fig. 5). Due to the strong seasonal difference in SSC values

355 (Sec. 4.4), net flux values were greater in summer than in winter—note different y-axis scales
 356 in Fig. 6.

357 Despite wide variations, average net fluxes at the bay-edge increased from BT1 inland
 358 to BT2 (BT3) in the summer (winter), indicating net erosion between these stations, and
 359 then decreased moving inland towards BT5 (Fig. 6), indicating net deposition. Net fluxes
 360 were more constant in x along the creek-edge transect, though typically decreased inland dur-
 361 ing high-flux inundations. Relative to less-organized patterns at the bay-edge, net fluxes at
 362 the creek transect were more clearly correlated with tidal depth (Fig. 6). The relationship
 363 between SSF and inundation depth was more pronounced in flood than ebb values. Thus,
 364 larger flood flux values (but stable ebb flux values) often drove larger net flux values for deeper
 365 inundations. Inundations in which SSC was high during the ebb drove the most negative net
 366 flux values: BT2 in the summer had a single negative net flux value, the result of an inun-
 367 dation on July 20, 2021 that coincided with the highest waves of the summer season, where
 368 both BT1 and BT2 had high ebb SSF values. The ≈ -500 g/m net flux value at BT1 in the
 369 winter season was from wave heights almost tripling over the course of the inundation, caus-
 370 ing greater resuspension during the ebb than flood.

371 5 Discussion

372 5.1 Approximating The Marsh Sediment Budget

373 Together, this work allows us to develop sediment budget of the marsh complex. We
 374 compare our tile-based deposition rates, fluxes, and flux-based deposition rates with marsh-
 375 edge erosion, and creek fluxes into Cargill Pond (Sec. 3.5) on transect (per-unit-width) and/or
 376 whole-marsh bases.

377 On a per-unit-width basis, the tile-based model predicted similar magnitudes of sed-
 378 iment import at both bay-edge and creek-edge transects, despite the higher per-area depo-
 379 sition rates along the creek transect (Table 2). This was due to a larger cross-shore region
 380 of elevated deposition in the $D(x)$ function at the bay-edge, which outweighed the narrow
 381 band of very high deposition by the creek banks. The interior-most stations (BT5/CT4) of
 382 both transects had similar average net flux values: $+0.27/+0.21$ (bay/creek) in summer and
 383 $+0.05/+0.05$ in winter, in kg/day/m (not included in table). These values make clear that
 384 large proportions of the sediment flux across BT1/CT1 flow through to BT5/CT4, or that
 385 there is resuspension within the sensor transects. The marsh-edge erosion rates (fourth line

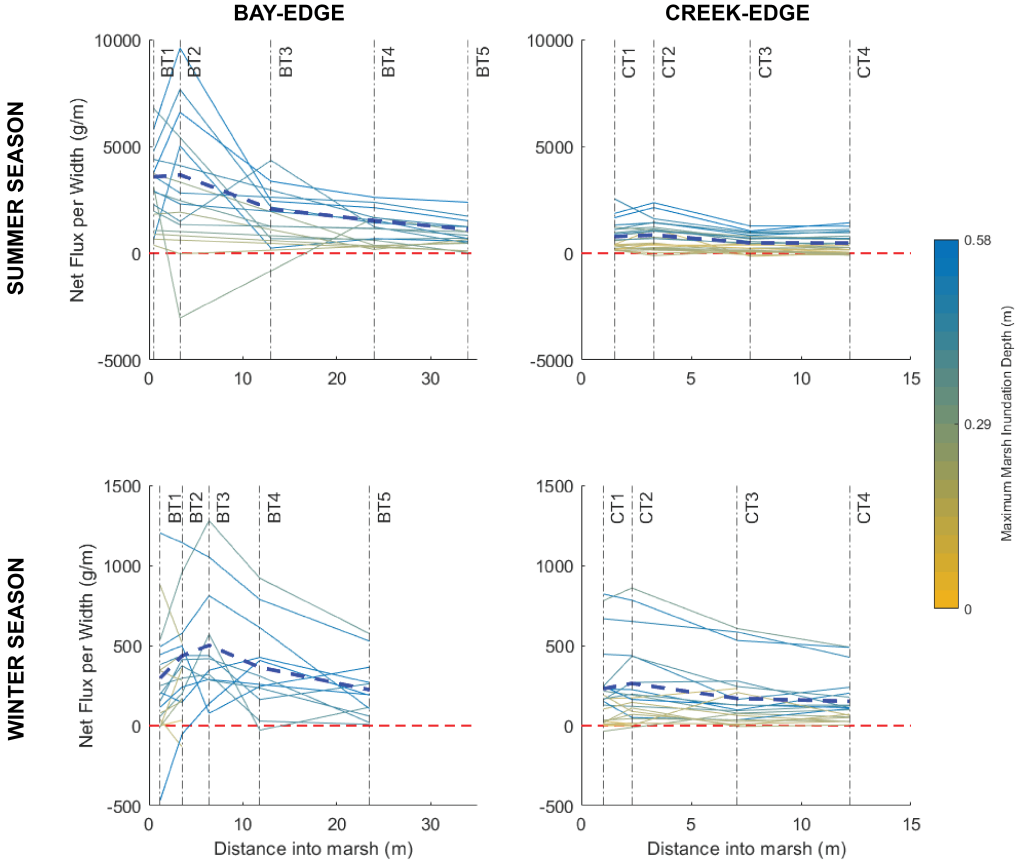


Figure 6. Net fluxes at each sensor are visualized on a *per-inundation basis*, where each line in the above figures represents one inundation of net SSF per unit width. The average of inundations in which every sensor recorded good data is represented by a thick dashed blue line. Note that the y-axis scale of the summer season is much different than that of the winter. The dotted red line drawn at zero differentiates net inland (+)/offshore (-) flux. Lines are colored by inundation depth, with blue representing relative maxima and maize representing relative minima. Note that lines may interpolate between sensors who did not have sufficient data for a given inundation.

Per-Width Deposition Rate ($\text{kg day}^{-1} \text{ m}^{-1}$)	Summer		Winter	
	Bay	Creek*	Bay	Creek*
Tile-Based Deposition Model	+0.96	+0.64	+0.07	+0.11
Net Flux Across Edge (BT1 or CT1)	+1.11	+0.34	+0.10	+0.09
Flux-Based Deposition + Net Flux to Interior (BT5 or CT4)	+0.45	+0.23	+0.05	+0.06
Bay Edge Lateral Erosion	-4.71		-1.35	

Whole-Marsh Import Rate (kg day^{-1})	Summer		Winter	
	Bay	Creeks	Bay	Creeks
Tile-Based Deposition Model	+1310	+4770	+98	+924
Bay Edge Lateral Erosion †	-6125		-1750	
Import to Cargill ‡		+5558		+311

Table 2. Mass import (+) or export (-) rates derived by various methods. The top half is on a per-unit-width-of-shoreline basis; the bottom half represents the entire marsh area. Tile deposition rates are the mean of spring and neap $D(x)$ curves. *These creek-side values represent only those of the primary channel, not data from the interior creek. †Derived from WinklerPrins et al. (2024). ‡Derived from Nowacki et al. (2024).

386 of Table 2) are relatively rapid, much greater than the mass of imported sediment (second
 387 line) at the edge.

388 At the scale of the entire marsh (Table 2 lower half), the extent of the tidal creek net-
 389 work caused creek-driven import to exceed bay-driven import by wide margins in both sea-
 390 sons. In the winter, the bay-edge tile-based import was an order-of-magnitude smaller than
 391 the creek-edge import. This was not purely a product of reduced nearshore SSC in the win-
 392 ter, as both bay-side and creek-side transects responded to nearshore SSC (Sec. 4.4). Instead,
 393 the lower wave climate in the winter season led to less sediment redistribution from the ero-
 394 sional edge to the marsh interior, whereas the mechanisms of import at the creek-edge re-
 395 mained consistent.

396 The four components in the second half of Table 2 represent the sediment budget of
 397 the WTMS+Cargill complex for each season. In the summer, their sum was +5513 kg/day
 398 (with heavy influence by import to Cargill); in the winter, -417 kg/day. There was a clear
 399 seasonal variation in each of the three components of the budget: much higher import and
 400 export rates in the summer than the winter. We attribute this to the intense sea breeze-driven
 401 waviness of the summer, which drove elevated SSC across the system via sediment resus-
 402 pension and rapid scarp retreat (Schoellhamer, 1996). Sediment-laden tidal inundations that
 403 flood the marsh and redistribution of sediment from the erosional edge both contribute to
 404 the accumulative interior, as in Lacy et al. (2020); Buffington et al. (2020). Low SSC val-
 405 ues in much of the winter study period—and rare alignment of high SSC with marsh-overtopping
 406 tides—made the net winter budget exporting by edge erosion. Because of the critical tim-
 407 ing between sediment in suspension and marsh-overtopping tides (Brand et al., 2010) and
 408 the high variability in the intensity of winter storms in California, different winter seasons may
 409 contribute very differently to the marsh sediment budget. It is yet to be seen whether a stormier
 410 winter would contribute more in sediment supply/import (as in Rosencranz et al. (2016, 2017)),
 411 in more rapid marsh-edge loss by storms, or if the two might effectively balance. We made
 412 visual observations of sediment on the tiles before and after approximately 4 inches of rain-
 413 fall between December 10th and 15th 2021, and qualitatively found that some sediment seemed
 414 to have been removed by the rain. This method might thus underestimate deposition dur-
 415 ing rainy periods, as the sediment may be redistributed across the marsh (Voulgaris & Mey-
 416 ers, 2004). While precipitation events and stream outflow are known to drive pulses of sed-
 417 iment into San Francisco Bay (Barnard et al., 2013), these large-scale dynamics may not reach

418 a small marsh disconnected from its upland environment like WTMS, or the effect of such
 419 events may be lagged and difficult to ascribe (Buffington et al., 2020).

420 At an annual scale, assuming summer/winter and spring/neap deposition rates are evenly
 421 distributed in time, WTMS imported +3500 kg/day via marsh-top deposition (Sec. 4.1); marsh-
 422 edge retreat analysis over an entire calendar year (Sec. 3.5) yielded -4600 kg/day; and the
 423 average of the two Cargill Pond import rates in Table 2 is \approx +2900 kg/day. These annual-
 424 scale values together sum to +1800 kg/day, so the marsh was net importing over our study
 425 year. Results from WinklerPrins et al. (2024), suggest the marsh eroded more rapidly in the
 426 fall and spring seasons than the winter and summer seasons (respectively). As edge erosion
 427 is largely a symptom of more waviness, which can drive more import, some ambiguity around
 428 the net annual budget remains due to reliance on only two seasonal values.

429 Using the representative marsh-top bulk density from Sec. 4.2, the annual-scale depo-
 430 sitional import at WTMS represents 3.5 mm/yr of vertical accretion. The region of the marsh
 431 has an \approx 4 mm/year subsidence rate (Shirzaei & Bürgmann, 2018), and local sea level rise
 432 of 1-2 mm/year (in addition to vertical land motion, based at the Golden Gate of San Fran-
 433 cisco Bay (*Sea Level Trends 9414290 San Francisco, California*, n.d.)). Thus, the marsh may
 434 not be keeping pace with relative sea level rise.

435 Despite annualized net sediment import and some accretion, WTMS is losing area at
 436 a rapid pace by marsh-scarp retreat (WinklerPrins et al., 2024), so this system is a case where
 437 lateral extent is sacrificed for vertical accretion (Hopkinson et al., 2018; Donatelli et al., 2020).
 438 Marsh instability is not uncommon: marsh landforms, especially rapidly eroding ones, are con-
 439 sidered non-equilibrium landscapes (Rahdarian et al., 2022; Fagherazzi et al., 2013; Kirwan
 440 & Murray, 2008). Our sediment budget suggests the Cargill Pond, protected by WTMS and
 441 levees, may effectively be serving as an accumulative “back marsh” for the erosional WTMS.
 442 The opening of the levee that separates WTMS and Cargill, part of an ongoing salt marsh
 443 restoration plan, connects WTMS to what is effectively an upland transition zone. These tra-
 444 jectories and Cargill’s vertical accretion rate are further explored in Nowacki et al. (2024).

445 In the following two sections, we discuss inundation-level patterns in sediment import/export,
 446 deposition/erosion, and redistribution across the marsh system using data from the marsh-
 447 top sensors in two ways. The first considers sediment deposition via particle settling, rep-
 448 resented by the “Deposition Potential” metric DP_i (Sec. 3.3), assuming that inundation du-
 449 ration and SSC over the marsh were primary controls on deposition rate (Lacy et al., 2018;

450 Duvall et al., 2019). We expected this method to perform better in regions dominated by
 451 sediment settling directly to the marsh top with low hydrodynamic disturbance. The second
 452 method imagines sediment fluxes through a control volume, using the gradient in sediment
 453 flux values to calculate a predicted deposition $D_{n,i}$ between two sensor stations. This model
 454 rests on the assumption of flow moving sequentially and between sensor stations BT1-5 and
 455 CT1-4, and was expected to perform better where sediment deposits as it flows over the marsh
 456 surface. Both methods can provide insight into daily-scale temporal variability, unlike the two-
 457 week tile-based deposition results.

458 5.2 Deposition via Sediment Settling

459 The relationships between DP and observed deposition were strong and very similar
 460 across the marsh interior stations (BT3-5, CT3-4), but deviated at BT1-2 and CT1-2 (Fig. 7).
 461 Relative to zero-intercept regressions of DP vs. tile data from the interior stations, DP at
 462 BT1 and BT2 often over-predicted the observed deposition rate from the tiles. DP at CT1
 463 and CT2 often under-predicted the observed deposition rate. The simplest explanation for
 464 these divergent patterns is the difference in the hydrodynamic regime: there was no wave
 465 influence at the creek-side transect. A characteristic difference between dynamics near the
 466 marsh-water boundaries and the marsh interior is consistent with findings by Coleman et al.
 467 (2020); Lacy et al. (2020); Buffington et al. (2020)

468 The inverse of the slope regressions (in Fig. 7) can be interpreted as effective settling
 469 velocities (w_s): they are 7.7×10^{-5} and 9.0×10^{-5} m/s from BT and CT, respectively. The
 470 95% confidence intervals of the two slopes overlap indicating similar settling regimes in the
 471 interiors of both transects. These w_s values are somewhat lower than that observed for floc-
 472 culi (micro/macrflocs) in the shallows of a nearby site in SSFB (Allen et al., 2024), but are
 473 consistent with modeling of sediment dynamics in SSFB which indicates the presence of a
 474 slow-settling class of particles (w_s of 1.4×10^{-5} m/s in Brand et al. (2015); w_s of 1×10^{-4}
 475 m/s in Chou et al. (2018)). This, in addition to the more spatially uniform SSC values in
 476 the marsh interior (Fig. 3)—as in Rosencranz et al. (2017)—indicates that it is this fine and
 477 slow-settling fraction which reaches the interior sensor stations (BT3-5, CT3-4) (Christiansen
 478 et al., 2000), and that settling is the dominant sediment transport process there (Stumpf,
 479 1983).

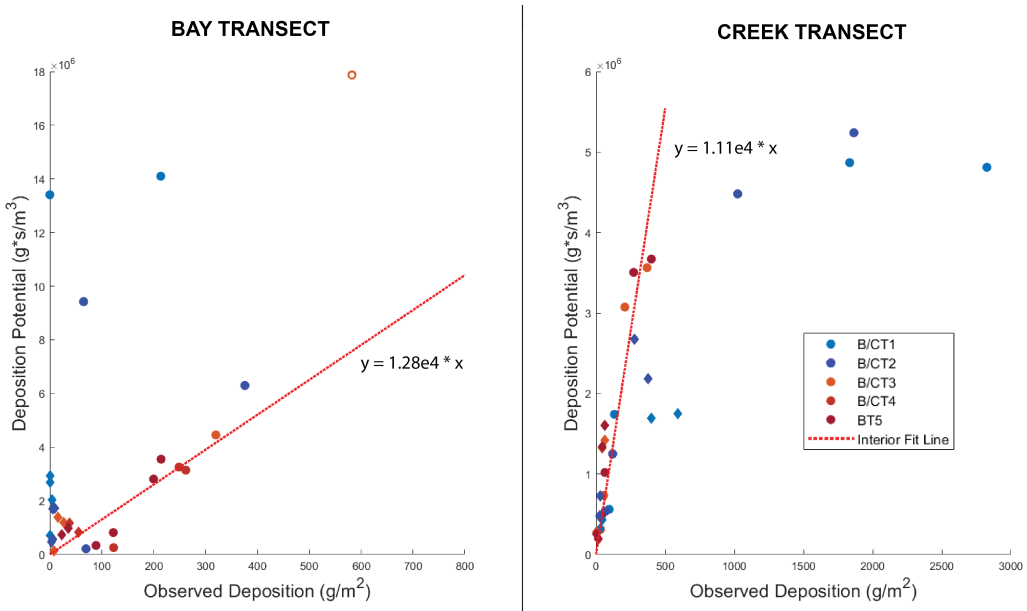


Figure 7. Deposition Potential metrics (summed over tile replacement periods) are plotted against observed tile deposition values (interpolated to our sensor locations). Round points are from the summer season; diamonds are from the winter. Dashed red lines were regressed to data from BT3-5 and CT3-4. The very high-valued DP point from BT3 in the summer (open circle) was excluded from the fit as it was a strong outlier.

480 The tiles closest to the bay-edge (near BT1-2), which often had zero observed depo-
 481 sition in the summer season, were the most wave-influenced. In the summer season especially,
 482 elevated SSC led to large DP , but the turbulent wave- and current-influenced environment
 483 at the bay interface prevented much sediment settling and often drove erosion (further dis-
 484 cussed in Sec. 5.3). At CT1-2, the deviation from the linear regression suggests a higher ef-
 485 fective settling velocity adjacent to the creek than farther inland. It is intuitive that the largest,
 486 heaviest flocs and sand particles would settle earliest during an inundation and more prox-
 487 imal to the edge: the greater sand fraction in marsh-top samples close to the bay and creek
 488 edge support this (Sec. 4.2). The creek-side edge was also much more vegetated than the
 489 erosional environment of the bay-side edge, helping slow flow and create an environment for
 490 deposition.

491 5.3 Deposition via Flux Gradient

492 Despite wide variations, per-inundation flux-gradient deposition ($D_{n,i}$) typically decreased
 493 to relatively near-zero magnitude with distance into the marsh, following the plateau-in-x net
 494 flux patterns from Sec. 4.5 (Fig. 8). Erosion and deposition were both suggested at the edge-
 495 most segments, with maximum deposition around 10 m into the marsh from the bay-edge
 496 and around 5 m from the creek-edge. In the summer at the bay-edge (top-left Fig. 8), the
 497 results for the two periods of spring tides were clearly different, with the first group notably
 498 net erosional between BT1-2 (and depositional between BT2-3) and the second group net
 499 depositional between BT1-3. The tile-based deposition exhibited the same pattern: the first
 500 set of spring tides was completely erosional at the first two tile locations; the second set was
 501 net depositional.

502 Negative (erosional) $D_{n,i}$ metrics were expected between BT1-2 from the tile results
 503 and the wave exposure, but also occurred at CT1-2. Inundations with erosion near the bound-
 504 aries tended to have regions of elevated deposition farther inland, particularly in the sum-
 505 mer season. The mass deposition inland of the erosional region during the first spring tides
 506 (plus net flux past BT5) was on average 180% of the mass eroded between BT1 and BT2,
 507 indicating that both redistributed and edge-imported sediment supply the marsh interior. This
 508 occurred in both seasons at the bay-edge transect, although with higher magnitudes in the
 509 summer, when the typically more powerful waves enhanced both resuspension and transport
 510 inland.

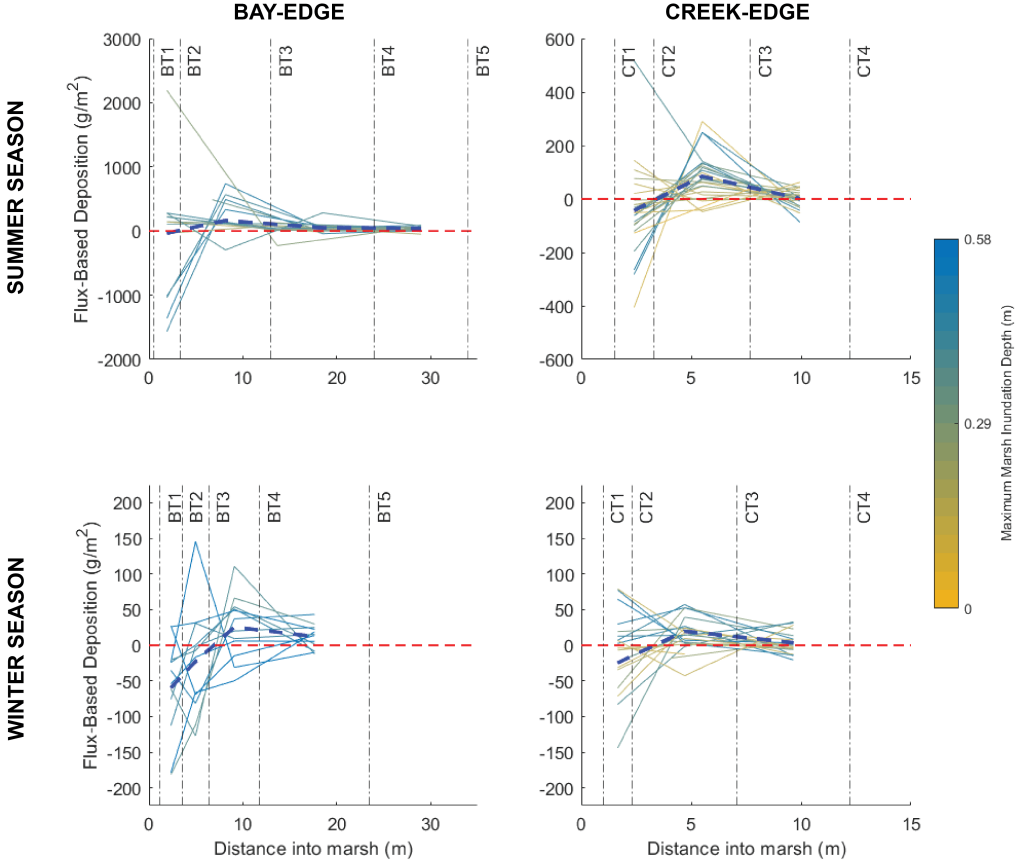


Figure 8. Net deposition/erosion per unit area on a *per inundation* basis, or $D_{n,i}$, values are shown, with each line representing an inundation. Dashed blue are averages of the inundations in which all sensors produced good data. NOTE that the panels generally have different Y-Axis scales. The dotted red line drawn at zero helps differentiate net change in regions between sensors, with deposition as positive and erosion as negative. Lines are colored by inundation depth, with blue representing relative maxima and maize representing relative minima. Note that lines may interpolate between sensors which did not have sufficient data for a given inundation.

At the creek-edge transect, the magnitudes of the erosion and deposition were similar in each season, suggesting more attribution to tidal flows. While the sensors closest to the creek were likely exposed to higher tidal velocities, the negative flux-based metrics ran in contrast to the high tile deposition rates observed near the creek-edge in both seasons (in Fig. 2). The dashed blue lines in Fig. 8 are averages based only on inundations during which all sensors recorded good data, typically the deeper inundations, which would be more likely to erode sediment near CT1. During many shallower inundations, the flux-based deposition metrics were positive between CT1-2. This variety implies the boundary regions between the marsh and the bay/creek can serve as temporary storage of sediment on tidal timescales.

Across the entire transects, the flux-based deposition rates—plus the net flux going inland at BT5/CT4—were the same order-of-magnitude but lower than the tile-based deposition rates (lines 1 vs 3 in Table. 2). This difference may simply be due to the tiles not documenting periods of erosion unless preceded by deposition. Vegetation may also capture sediment from the water column (Stein et al., 2021), preventing suspended sediment from reaching the marsh surface, but efficiency in interception of suspended sediments is low, likely < 1% (Wingenroth et al., 2021; Huang et al., 2008). Additionally, drainage patterns over the marsh surface are not precisely known: flood tide may not necessarily be entirely importing, and ebb not entirely exporting. Over our study, we observed a tendency for the marsh to seemingly flood from the bay-edge, and ebb through the primary creek. The lag time between peak inundations at the bay-edge and creek-edge transects suggest the bay-side floods and ebbs earlier than the creek. After high water, we suspect the subtle “levee” near BT2-3 (Fig. 1.D) encourages water to drain inland and ultimately ebb through the creek network rather than off the bay-side. Thus, $D_{n,i}$ metrics may have overpredicted sediment export from the marsh on ebb, biasing the values low. Lastly, we did not capture extremely shallow flows (typically below 10 cm) over the marsh-top due to sensor positioning and data cleaning needs. Shi et al. (2019) have suggested that these very shallow flows may have outsize impact on the hydrodynamics and sedimentation patterns in mudflats, and the same may be true on marsh-top platforms. Despite these caveats, order-of-magnitude agreement in sediment import from all the methods presented here increases confidence in our results.

540 5.4 Conceptual Model of Marsh-Top Sediment Dynamics

541 Sediment is imported onto the marsh by overtopping tidal inundations, with water entering the marsh from both bay-edge and tidal creeks. The bay-side of the marsh has an ≈

543 2 m region of almost no vegetation due to the wave climate, where sediment is deposited
 544 and eroded, but mostly eroded and carried inland. The region of maximum deposition is ≈
 545 6 m into the marsh from the bay-edge, reflecting >90% attenuation of wave energy, more
 546 vegetation cover, and the redistribution of sediment away from the bay-edge. At the creek-
 547 edge, deposition is high immediately adjacent to the creek and quickly tapers with distance,
 548 as heavy flocs and sand particles settle out of vegetation-slowed water. Still, some erosion
 549 and redistribution occurs near the creek-edge, attributable to strong tidal currents. There
 550 are similar proportions of sand and clay on the marsh-top at bay-side and creek-side regions.
 551 All of these factors contribute to viewing the bay-side transect as analogous to the creek-
 552 side transect, but transposed ≈ 6 meters inland to a more elongated cross-shore zone of el-
 553 evated deposition due to wave-driven redistribution, similar to what was found by Duvall et
 554 al. (2019); Elsey-Quirk et al. (2019). Across the marsh, deposition rates decrease exponen-
 555 tially with distance into the marsh interior (as found by Duvall et al. (2019) at bay-edge and
 556 Moskalski and Sommerfield (2012) at creek-edge). The interior of the marsh, insulated from
 557 strong wave and tidal hydrodynamics, receives fine “wash load” sediments from the edges.
 558 Deposition rates here reflect available suspended-sediment in the water column and tidal du-
 559 rations over which sediment can settle to the surface.

560 6 Conclusion

561 A wave-exposed and laterally-eroding marsh in South San Francisco Bay imported large
 562 proportions of sediment via both its bay edge and tidal creeks, although on a marsh-wide ba-
 563 sis, the tidal creeks contributed approximately four times more sediment. The summer, typ-
 564 ically much higher in wave energy than the winter, accounted for the largest edge erosion
 565 rate and flux import into the marsh. Waves in the adjacent bay drove resuspension, raising
 566 suspended-sediment concentrations and leading to higher deposition rates throughout the
 567 marsh.

568 The sediment budget of the Whale’s Tail Marsh and Cargill Pond system was net im-
 569 porting in the summer season and net exporting, at a slower rate, in the winter. An annual-
 570 scale analysis suggested net import of sediment over the study year, and this led to vertical
 571 accretion across the marsh surfaces. Despite this vertical accretion, the marsh is shrinking
 572 in area through lateral erosion. The long-term sediment budget remains uncertain because
 573 of the highly variable winter storm regime in California. On the marsh surface, our study showed
 574 that sediment may be remobilized from erosional regions to depositional regions, dependent

575 on both wave- and tide-driven hydrodynamics. Thus, a marsh with a positive sediment bud-
 576 get may still be undergoing rapid loss of area and internal redistribution of sediment. Max-
 577 imum net deposition occurred within 10 meters of the water boundaries (either bay or tidal
 578 creek), although at the bay edge the zone of maximum net deposition was inland of a wave-
 579 exposed erosional region. The interior of the marsh accumulated sediment very slowly and
 580 was dominated by settling of suspended sediment.

581 Interventions seeking to mitigate erosion of marshy shorelines must be cautious not to
 582 disconnect the marsh-top surface from the redistribution potential of waves or the suspended-
 583 sediment resources from the shallows. Care should be given to the possible strong seasonal
 584 patterns of these dynamics in planning management actions.

585 Appendix A Appendix: Supporting Methods Figures

586 A1 Marsh-Top Hydrologic Segmentation

587 By hand, lines representing the bay-edge boundary and creek channels were drawn. Only
 588 creek channels that remained wet during lower-low tides of aerial imagery collection were drawn.
 589 The bay-edge curve was placed immediately at the marsh-scarp boundary; for the channels,
 590 curves were drawn through the center, and offsets were established to account for the dis-
 591 tance from center to creek bank. Using GIS software, a 1 m-spaced grid of points was set
 592 over the extent of WTMS. The grid points were then associated with their nearest geographic
 593 "water boundary curve". This thus segmented the marsh surface into regions (Fig. A1) at-
 594 tributable to different proximal sources of water.

595 These regions were then associated with appropriate $D(x)$ curves (bay-edge, primary
 596 channel, or tertiary channel). The three blue areas in the eastern half of the marsh, as well
 597 as the sea green region in the northwest, used the curve fit to the primary creek tile data;
 598 the five tertiary creeks (lime, chartreuse, orange, rust, and red) were fit to the tiles in the
 599 interior transect. The small maroon region in the northwest and the purple western edge were
 600 fit to the $D(x)$ curve from the bay-edge.

601 A2 Inundation Detection Algorithm

602 Unexpected aberrations in pressure records, up to 0.3 dbar in magnitude, were observed
 603 while sensors were not inundated, attributed to temperature-dependent response of the pres-
 604 sure sensors. Although these were noticed explicitly during dry periods, the discrepancies led

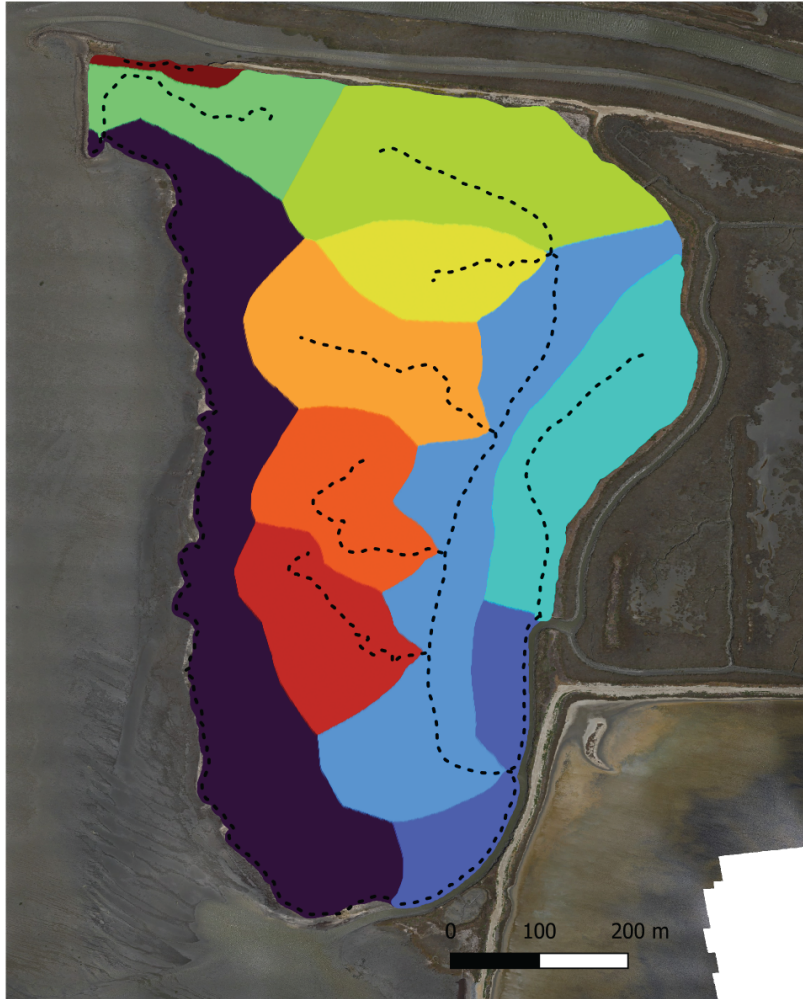


Figure A1. Surface of Whale's Tail Marsh colored by the presumed body of water that inundates the given regions of the marsh, based on shortest distance to water feature (black dotted lines). Note that the only included creeks were those that retained water through lower low tides.

605 to concern over the accuracy of pressure data to reflect water depths across sensors. To ad-
 606 just for this, we used the sensor with the smallest pressure deviation (based on lab tests) as
 607 a “master sensor” to represent water depths in each season. Once the master sensor’s ad-
 608 justment factor was applied, we assumed all sensors had equal water surface elevations at
 609 the highest observed high tide in each study season. Thus we applied depth adjustment fac-
 610 tors to each sensor in each season, to match the master sensor’s water surface elevation at
 611 the highest-tide moment in each season.

612 To detect marsh-top inundations at each marsh-top sensor (BT1-5 and CT1-4), a com-
 613 bination of the co-located pressure record and SSC record were used, schematized in Fig. A2.
 614 The algorithm found peaks in the pressure record, then searched around the associated times-
 615 tamps for SSC signals above low thresholds to identify beginnings (10 mg/L threshold) and
 616 ends (3 mg/L threshold) of inundations. Finding aligned peaks in pressure *and* SSC helped
 617 avoid false high-pressure events, visible in dry periods in the lower panel of Fig. A2. Inun-
 618 dation periods were split into “flood” and “ebb” periods at the datestamp of the highest pres-
 619 sure (and water level) value for that inundation, and mean SSC values (following outlier re-
 620 moval) were calculated for both flood and ebb, in addition to a whole-inundation mean. The
 621 time inundated for each inundation T_i was calculated by fitting a $d = a*(t-b)^2+c$ curve
 622 onto each inundation’s depth $d(t)$ timeseries, and taking the time elapsed between the ze-
 623 ros of the concave-down parabola, thus accounting for the pressure sensors’ variable heights
 624 above bed.

625 References

- 626 Allen, R., Livsey, D., & McGill, S. (2024). Observations of flocs in an estuary and im-
 627 plications for computation of settling velocity [accepted for publication in JGR:
 628 Oceans]. *U.S. Geological Survey*.
- 629 Barbier, E. B., Hacker, S. D., Kennedy, C., Koch, E. W., Stier, A. C., & Silliman,
 630 B. R. (2011, May). The value of estuarine and coastal ecosystem ser-
 631 vices. *Ecological Monographs*, 81(2), 169–193. Retrieved 2023-12-03, from
 632 <http://doi.wiley.com/10.1890/10-1510.1> doi: 10.1890/10-1510.1
- 633 Barnard, P. L., Schoellhamer, D. H., Jaffe, B. E., & McKee, L. J. (2013, Novem-
 634 ber). Sediment transport in the San Francisco Bay Coastal System: An
 635 overview. *Marine Geology*, 345, 3–17. Retrieved 2022-12-18, from <https://linkinghub.elsevier.com/retrieve/pii/S0025322713000376> doi:

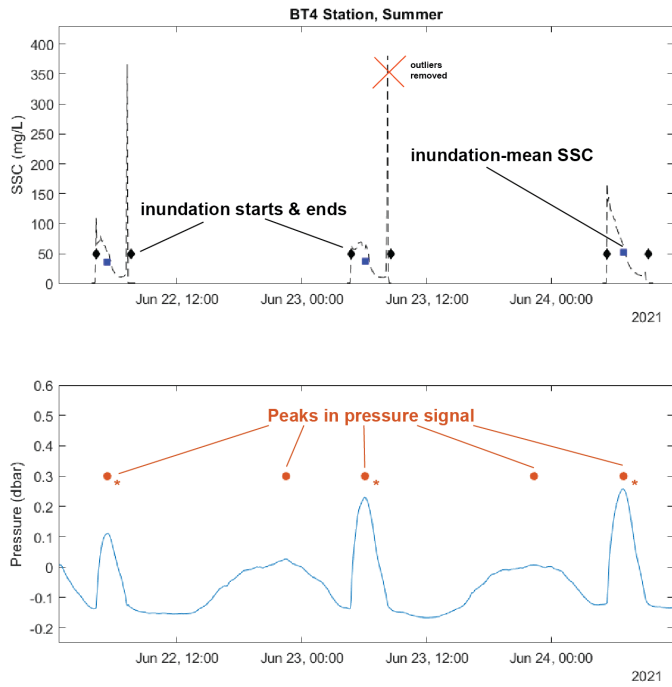


Figure A2. Description of the algorithm for inundation-detection, using a subset of the BT4 timeseries data. Peaks in the pressure signal are identified first (lower panel), and then the SSC signal is searched to identify which pressure peaks were likely real inundations (demarcated with *). From the SSC timeseries, starts and ends of inundations were detected with low thresholds, outlier bursts were removed, and flood/ebb/whole-inundation mean SSC values were found.

- 637 10.1016/j.margeo.2013.04.005
- 638 Brand, A., Lacy, J. R., Gladding, S., Holleman, R., & Stacey, M. (2015, March).
 639 Model-based interpretation of sediment concentration and vertical flux mea-
 640 surements in a shallow estuarine environment: Shallow estuarine sediment dy-
 641 namics. *Limnology and Oceanography*, 60(2), 463–481. Retrieved 2024-06-13,
 642 from <https://onlinelibrary.wiley.com/doi/10.1002/lno.10047> doi:
 643 10.1002/lno.10047
- 644 Brand, A., Lacy, J. R., Hsu, K., Hoover, D., Gladding, S., & Stacey, M. T. (2010,
 645 November). Wind-enhanced resuspension in the shallow waters of South San Fran-
 646 cisco Bay: Mechanisms and potential implications for cohesive sediment transport.
 647 *Journal of Geophysical Research*, 115(C11), C11024. Retrieved 2023-04-11, from
 648 <http://doi.wiley.com/10.1029/2010JC006172> doi: 10.1029/2010JC006172
- 649 Buffington, K. J., Dugger, B. D., Thorne, K. M., & Takekawa, J. Y. (2016, December).
 650 Statistical correction of lidar-derived digital elevation models with multispectral
 651 airborne imagery in tidal marshes. *Remote Sensing of Environment*, 186, 616–625.
 652 Retrieved 2021-12-08, from <https://linkinghub.elsevier.com/retrieve/pii/S0034425716303637> doi: 10.1016/j.rse.2016.09.020
- 653 Buffington, K. J., Janousek, C. N., Thorne, K. M., & Dugger, B. D. (2020, Oc-
 654 tober). Spatiotemporal Patterns of Mineral and Organic Matter Deposition
 655 Across Two San Francisco Bay-Delta Tidal Marshes. *Wetlands*, 40(5), 1395–
 656 1407. Retrieved 2024-05-07, from <https://link.springer.com/10.1007/s13157-019-01259-3> doi: 10.1007/s13157-019-01259-3
- 657 Chou, Y., Nelson, K. S., Holleman, R. C., Fringer, O. B., Stacey, M. T., Lacy, J. R.,
 658 ... Koseff, J. R. (2018, June). Three-Dimensional Modeling of Fine Sed-
 659 iment Transport by Waves and Currents in a Shallow Estuary. *Journal of Geo-
 660 physical Research: Oceans*, 123(6), 4177–4199. Retrieved 2024-06-13, from
 661 <https://agupubs.onlinelibrary.wiley.com/doi/10.1029/2017JC013064>
 662 doi: 10.1029/2017JC013064
- 663 Christiansen, T., Wiberg, P., & Milligan, T. (2000, March). Flow and Sediment Trans-
 664 port on a Tidal Salt Marsh Surface. *Estuarine, Coastal and Shelf Science*, 50(3),
 665 315–331. Retrieved 2023-10-12, from <https://linkinghub.elsevier.com/retrieve/pii/S0272771400905481> doi: 10.1006/ecss.2000.0548
- 666 Coleman, D. J., Ganju, N. K., & Kirwan, M. L. (2020, August). Sediment Delivery to a

- 670 Tidal Marsh Platform Is Minimized by Source Decoupling and Flux Convergence.
 671 *Journal of Geophysical Research: Earth Surface*, 125(8), e2020JF005558. Retrieved
 672 2024-04-14, from <https://agupubs.onlinelibrary.wiley.com/doi/10.1029/2020JF005558> doi: 10.1029/2020JF005558
- 673 Conomos, T. J., Smith, R. E., & Gartner, J. W. (1985). Environmental setting of San
 674 Francisco Bay. *Hydrobiologia*, 129. doi: <https://doi.org/10.1007/BF00048684>
- 675 Donatelli, C., Kalra, T. S., Fagherazzi, S., Zhang, X., & Leonardi, N. (2020, December).
 676 Dynamics of Marsh-Derived Sediments in Lagoon-Type Estuaries. *Journal of Geophysical Research: Earth Surface*, 125(12), e2020JF005751. Retrieved 2024-04-14, from <https://agupubs.onlinelibrary.wiley.com/doi/10.1029/2020JF005751> doi: 10.1029/2020JF005751
- 677 Duvall, M. S., Wiberg, P. L., & Kirwan, M. L. (2019, March). Controls on Sediment
 678 Suspension, Flux, and Marsh Deposition near a Bay-Marsh Boundary. *Estuaries and Coasts*, 42(2), 403–424. Retrieved 2021-04-30, from
 679 <http://link.springer.com/10.1007/s12237-018-0478-4> doi: 10.1007/s12237-018-0478-4
- 680 Elsey-Quirk, T., Mariotti, G., Valentine, K., & Raper, K. (2019, April). Retreating marsh
 681 shoreline creates hotspots of high-marsh plant diversity. *Scientific Reports*, 9(1), 5795. Retrieved 2023-11-20, from <https://www.nature.com/articles/s41598-019-42119-8> doi: 10.1038/s41598-019-42119-8
- 682 Fagherazzi, S., Mariotti, G., Wiberg, P., & McGlathery, K. (2013, September).
 683 Marsh Collapse Does Not Require Sea Level Rise. *Oceanography*, 26(3), 70–77. Retrieved 2021-10-25, from <https://tos.org/oceanography/article/marsh-collapse-does-not-require-sea-level-rise> doi: 10.5670/oceanog.2013.47
- 684 Ferreira, J. C. T., Lacy, J. R., McGill, S. C., WinklerPrins, L. T., Nowacki, D. J.,
 685 Stevens, A. W., & Tan, A. C. (2023). *Hydrodynamic and sediment transport data from Whale's Tail marsh and adjacent waters in South San Francisco Bay, California 2021-2022*. Retrieved 2023-05-16, from <https://cmgds.marine.usgs.gov/data-releases/datarelease/10.5066/P972R6AW/> (Publisher: U.S. Geological Survey) doi: 10.5066/P972R6AW
- 686 Ferreira, J. C. T., McGill, S. C., Tan, A. C., & Lacy, J. R. (2023). *Grain size, bulk
 687 density, and carbon content of sediment collected from Whale's Tail South marsh*

- 703 and adjacent bay floor, South San Francisco Bay, California, 2021-2022. U.S. Ge-
 704 ological Survey. Retrieved 2024-05-31, from <https://cmgds.marine.usgs.gov/>
 705 data-releases/datarelease/10.5066/P98BL0XF/ doi: 10.5066/P98BL0XF
- 706 Gabet, E. J. (1998, December). Lateral Migration and Bank Erosion in a Saltmarsh
 707 Tidal Channel in San Francisco Bay, California. *Estuaries*, 21(4), 745. Re-
 708 trieved 2021-09-09, from <http://link.springer.com/10.2307/1353278> doi:
 709 10.2307/1353278
- 710 Ganju, N. K. (2019, June). Marshes Are the New Beaches: Integrating Sediment Trans-
 711 port into Restoration Planning. *Estuaries and Coasts*, 42(4), 917–926. Retrieved
 712 2021-12-08, from <http://link.springer.com/10.1007/s12237-019-00531-3>
 713 doi: 10.1007/s12237-019-00531-3
- 714 Hopkinson, C. S., Morris, J. T., Fagherazzi, S., Wollheim, W. M., & Raymond, P. A.
 715 (2018, August). Lateral Marsh Edge Erosion as a Source of Sediments for Vertical
 716 Marsh Accretion. *Journal of Geophysical Research: Biogeosciences*, 123(8), 2444–
 717 2465. Retrieved 2021-09-09, from <https://onlinelibrary.wiley.com/doi/10.1029/2017JG004358> doi: 10.1029/2017JG004358
- 719 Huang, Y. H., Saiers, J. E., Harvey, J. W., Noe, G. B., & Mylon, S. (2008, April). Ad-
 720 vection, dispersion, and filtration of fine particles within emergent vegetation of
 721 the Florida Everglades. *Water Resources Research*, 44(4), 2007WR006290. Re-
 722 trieved 2023-12-09, from <https://agupubs.onlinelibrary.wiley.com/doi/10.1029/2007WR006290> doi: 10.1029/2007WR006290
- 724 Kirwan, M. L., & Murray, A. B. (2008, December). Tidal marshes as disequilibrium
 725 landscapes? Lags between morphology and Holocene sea level change. *Geophys-
 726 ical Research Letters*, 35(24), L24401. Retrieved 2022-01-10, from <http://doi.wiley.com/10.1029/2008GL036050> doi: 10.1029/2008GL036050
- 728 Lacy, J. R., Ferner, M. C., & Callaway, J. C. (2018, September). The influence
 729 of neap–spring tidal variation and wave energy on sediment flux in salt marsh
 730 tidal creeks. *Earth Surface Processes and Landforms*, 43(11), 2384–2396. Re-
 731 trieved 2023-11-22, from <https://onlinelibrary.wiley.com/doi/10.1002/esp.4401> doi: 10.1002/esp.4401
- 733 Lacy, J. R., Foster-Martinez, M. R., Allen, R. M., Ferner, M. C., & Callaway, J. C.
 734 (2020, January). Seasonal Variation in Sediment Delivery Across the Bay-Marsh
 735 Interface of an Estuarine Salt Marsh. *Journal of Geophysical Research: Oceans*,

- 736 125(1). Retrieved 2021-12-09, from <https://onlinelibrary.wiley.com/doi/abs/10.1029/2019JC015268> doi: 10.1029/2019JC015268
- 737
738 Larsen, L. G., & Milligan, B. (2023, December). Sediment austerity is the new coastal
739 norm. *Science*, 382(6675), 1123–1124. Retrieved 2023-12-11, from <https://www.science.org/doi/10.1126/science.adl4251> doi: 10.1126/science.adl4251
- 740
741 Liu, Z., Fagherazzi, S., & Cui, B. (2021, February). Success of coastal wetlands restora-
742 tion is driven by sediment availability. *Communications Earth & Environment*,
743 2(1), 44. Retrieved 2023-10-12, from <https://www.nature.com/articles/s43247-021-00117-7> doi: 10.1038/s43247-021-00117-7
- 744
745 Logan, J., Winklerprins, L. T., & Lacy, J. R. (2023). *Structure-from-motion derived*
746 *orthomosaic imagery and digital surface models (DSMs) from the intertidal region*
747 *at Whale's Tail Marsh, South San Francisco Bay, CA.* U.S. Geological Survey.
748 Retrieved 2023-05-16, from <https://www.sciencebase.gov/catalog/item/6308060ad34e3b967a8c15c7> doi: 10.5066/P9L9R2VS
- 749
750 Mariotti, G., & Carr, J. (2014, April). Dual role of salt marsh retreat: Long-term loss
751 and short-term resilience. *Water Resources Research*, 50(4), 2963–2974. Re-
752 tried 2021-09-30, from <http://doi.wiley.com/10.1002/2013WR014676> doi:
753 10.1002/2013WR014676
- 754
755 Moskalski, S. M., & Sommerfield, C. K. (2012, February). Suspended sediment deposi-
756 tion and trapping efficiency in a Delaware salt marsh. *Geomorphology*, 139-140,
757 195–204. Retrieved 2021-04-23, from <https://linkinghub.elsevier.com/retrieve/pii/S0169555X11005344> doi: 10.1016/j.geomorph.2011.10.018
- 758
759 Nowacki, D. J., & Ganju, N. K. (2020, November). Sediment Dynamics of a Divergent
760 Bay–Marsh Complex. *Estuaries and Coasts*. Retrieved 2021-05-05, from <http://link.springer.com/10.1007/s12237-020-00855-5> doi: 10.1007/s12237-020-00855-5
- 761
762 Nowacki, D. J., Lacy, J. R., & La Selle, S. M. (2024). Linking tidal-creek sediment
763 fluxes to vertical sediment accumulation in a restored salt marsh [submitted to
764 *ESPL*].
- 765
766 Rahdarian, A., Bryan, K. R., & Van Der Wegen, M. (2022, August). On the Influence
767 of Antecedent Morphology on Development of Equilibrium Bathymetry in Estuaries
768 Past and Future. *Journal of Geophysical Research: Earth Surface*, 127(8). Re-
trieved 2022-12-18, from <https://onlinelibrary.wiley.com/doi/10.1029/>

- 769 2022JF006621 doi: 10.1029/2022JF006621
- 770 Reed, D. J. (1988, January). Sediment dynamics and deposition in a retreating
 771 coastal salt marsh. *Estuarine, Coastal and Shelf Science*, 26(1), 67–79. Retrieved
 772 2023-07-26, from <https://linkinghub.elsevier.com/retrieve/pii/0272771488900121> doi: 10.1016/0272-7714(88)90012-1
- 773
- 774 Rosencranz, J. A., Brown, L. N., Holmquist, J. R., Sanchez, Y., MacDonald, G. M.,
 775 & Ambrose, R. F. (2017, September). The Role of Sediment Dynamics for
 776 Inorganic Accretion Patterns in Southern California's Mediterranean-Climate
 777 Salt Marshes. *Estuaries and Coasts*, 40(5), 1371–1384. Retrieved 2023-12-
 778 07, from <http://link.springer.com/10.1007/s12237-017-0224-3> doi:
 779 10.1007/s12237-017-0224-3
- 780 Rosencranz, J. A., Ganju, N. K., Ambrose, R. F., Brosnahan, S. M., Dickhudt,
 781 P. J., Guntenspergen, G. R., ... Thorne, K. M. (2016, July). Balanced
 782 Sediment Fluxes in Southern California's Mediterranean-Climate Zone Salt
 783 Marshes. *Estuaries and Coasts*, 39(4), 1035–1049. Retrieved 2023-12-07,
 784 from <http://link.springer.com/10.1007/s12237-015-0056-y> doi:
 785 10.1007/s12237-015-0056-y
- 786 Schile, L. M., Callaway, J. C., Morris, J. T., Stralberg, D., Parker, V. T., & Kelly, M.
 787 (2014, February). Modeling Tidal Marsh Distribution with Sea-Level Rise: Evalu-
 788 ating the Role of Vegetation, Sediment, and Upland Habitat in Marsh Resiliency.
 789 *PLoS ONE*, 9(2), e88760. Retrieved 2021-12-24, from <https://dx.plos.org/10.1371/journal.pone.0088760> doi: 10.1371/journal.pone.0088760
- 790
- 791 Schoellhamer, D. H. (1996, May). Factors affecting suspended-solids concen-
 792 trations in South San Francisco Bay, California. *Journal of Geophysical
 793 Research: Oceans*, 101(C5), 12087–12095. Retrieved 2024-04-14, from
 794 <https://agupubs.onlinelibrary.wiley.com/doi/10.1029/96JC00747>
 795 doi: 10.1029/96JC00747
- 796 *Sea Level Trends 9414290 San Francisco, California.* (n.d.). Retrieved 2024-07-04, from
 797 https://tidesandcurrents.noaa.gov/slrends/slrends_station.shtml?id=9414290
- 798
- 799 Shi, B., Cooper, J. R., Li, J., Yang, Y., Yang, S., Luo, F., ... Wang, Y. P. (2019,
 800 June). Hydrodynamics, erosion and accretion of intertidal mudflats in extremely
 801 shallow waters. *Journal of Hydrology*, 573, 31–39. Retrieved 2022-11-23, from

- 802 <https://linkinghub.elsevier.com/retrieve/pii/S002216941930294X> doi:
 803 10.1016/j.jhydrol.2019.03.065
- 804 Shirzaei, M., & Bürgmann, R. (2018, March). Global climate change and local land
 805 subsidence exacerbate inundation risk to the San Francisco Bay Area. *Science*
 806 *Advances*, 4(3), eaap9234. Retrieved 2023-04-10, from <https://www.science.org/doi/10.1126/sciadv.aap9234> doi: 10.1126/sciadv.aap9234
- 807 Smith, K. E., Terrano, J. F., Khan, N. S., Smith, C. G., & Pitchford, J. L. (2021,
 808 September). Lateral shoreline erosion and shore-proximal sediment deposition on a
 809 coastal marsh from seasonal, storm and decadal measurements. *Geomorphology*,
 810 389, 107829. Retrieved 2023-10-12, from <https://linkinghub.elsevier.com/retrieve/pii/S0169555X21002373> doi: 10.1016/j.geomorph.2021.107829
- 811 Stein, S., Wingenroth, J., & Larsen, L. (2021, April). A Functional Form for Fine Sediment
 812 Interception in Vegetated Environments. *Geosciences*, 11(4), 157. Retrieved
 813 2021-04-23, from <https://www.mdpi.com/2076-3263/11/4/157> doi: 10.3390/geosciences11040157
- 814 Stralberg, D., Brennan, M., Callaway, J. C., Wood, J. K., Schile, L. M., Jongsomjit,
 815 D., ... Crooks, S. (2011, November). Evaluating Tidal Marsh Sustainability in the Face of Sea-Level Rise: A Hybrid Modeling Approach Applied
 816 to San Francisco Bay. *PLoS ONE*, 6(11), e27388. Retrieved 2021-12-
 817 24, from <https://dx.plos.org/10.1371/journal.pone.0027388> doi:
 818 10.1371/journal.pone.0027388
- 819 Stumpf, R. P. (1983, November). The process of sedimentation on the surface
 820 of a salt marsh. *Estuarine, Coastal and Shelf Science*, 17(5), 495–508. Retrieved
 821 2023-12-12, from <https://linkinghub.elsevier.com/retrieve/pii/0272771483900021> doi: 10.1016/0272-7714(83)90002-1
- 822 Thorne, K. M., & Bristow, M. L. (2023). *Sediment deposition and accretion data from a tidal salt marsh in South San Francisco Bay, California 2021-2022*. U.S. Geological Survey. Retrieved 2023-11-20, from <https://www.sciencebase.gov/catalog/item/64ff51e4d34ed30c2057b3ae> doi: 10.5066/P9YBBXIZ
- 823 Voulgaris, G., & Meyers, S. T. (2004, June). Net effect of rainfall activity on salt-marsh
 824 sediment distribution. *Marine Geology*, 207(1-4), 115–129. Retrieved 2024-06-17,
 825 from <https://linkinghub.elsevier.com/retrieve/pii/S0025322704000751>
 826 doi: 10.1016/j.margeo.2004.03.009

- 835 Wiberg, P. L., & Sherwood, C. R. (2008, October). Calculating wave-generated bot-
836 tom orbital velocities from surface-wave parameters. *Computers & Geosciences*,
837 34(10), 1243–1262. Retrieved 2021-03-15, from <https://linkinghub.elsevier.com/retrieve/pii/S009830040800054X> doi: 10.1016/j.cageo.2008.02.010
- 838
839 Wingenroth, J., Yee, C., Nghiem, J., & Larsen, L. (2021, March). Effects of Stem Den-
840 sity and Reynolds Number on Fine Sediment Interception by Emergent Vegetation.
841 *Geosciences*, 11(3), 136. Retrieved 2023-12-08, from <https://www.mdpi.com/2076-3263/11/3/136> doi: 10.3390/geosciences11030136
- 842
843 WinklerPrins, L., Lacy, J. R., Stacey, M. T., Logan, J. B., & Stevens, A. W. (2024,
844 July). Seasonality of Retreat Rate of a Wave-Exposed Marsh Edge. *Journal of
845 Geophysical Research: Earth Surface*, 129(7). doi: <https://doi.org/10.1029/2023JF007468>
- 846